







Nano-clustering mediates phase transitions in a diastereomerically-stabilized ferroelectric nematic system

Hiroya Nishikawa¹, Koki Sano^{1,3}, Saburo Kurihara², Go Watanabe², Atsuko Nihonyanagi¹, Barun Dhara¹ & Fumito Araoka¹

In recent years, ferroelectric nematic liquid crystals have attracted considerable attention owing to their unique properties such as a colossal polarization, high electro-optic activity, and high fluidity. However, despite large efforts in designing and developing new ferrofluid molecules based on molecular parameters, the control and stabilization of ferroelectric nematic phase transitions remain challenging. Here, we discuss the impact of mixing 1,3-dioxane-tethered fluorinated (DIO) diastereomer molecules, namely *trans*DIO and *cis*DIO, in controlling the ferroelectric nematic phase transition, using X-ray diffraction to investigate the effect of smectic cybotactic cluster formation. Our results show that the ferroelectric nematic phase transition can be tuned by a smooth exchange of the ferroelectric nematic *trans*DIO and non-liquid crystal *cis*DIO components, where the similar dipole and molecular backbone of the two components ensures a consistent macroscopic polarization of the diastereomerically-controlled ferroelectric nematic phase.

¹RIKEN Center for Emergent Matter Science (CEMS), 2-1 Hirosawa, Wako, Saitama 351-0198, Japan. ²Department of Physics, School of Science, Kitasato University, 1-15-1 Kitasato, Sagamihara, Kanagawa 252-0373, Japan. ³Present address: Department of Chemistry and Materials, Faculty of Textile Science and Technology, Shinshu University, 3-15-1 Tokida, Ueda, Nagano 386-8567, Japan. ✉email: hiroya.nishikawa@riken.jp; fumito.araoka@riken.jp

Since the discovery of a true three-dimensional (3D) fluid ferroelectric nematic (N_F) phase showing a field-induced polarization reversal via a domain wall motion in liquid crystals (LCs), great interest has been dedicated to both fundamental science and applications^{1–35}. In the N_F phase, the inversion symmetry of the nematic (N) director is broken, forming macroscopic domains with a uniform polarization (P) along the director, n

(Fig. 1a). The striking features of N_F LCs are their large spontaneous polarization, gigantic dielectric permittivity^{3,13,14,18,21,24,28}, high nonlinear optical activity^{3,9,24,31}, electro-optic response with very low or zero threshold voltage^{8,12,13,15,17,20,22}, and high fluidity^{3,8,27} that may lead to unconventional soft matter technologies. According to the simple model by Born, the electric-dipolar interaction proportional to the square of the dipole moment, μ , which should be

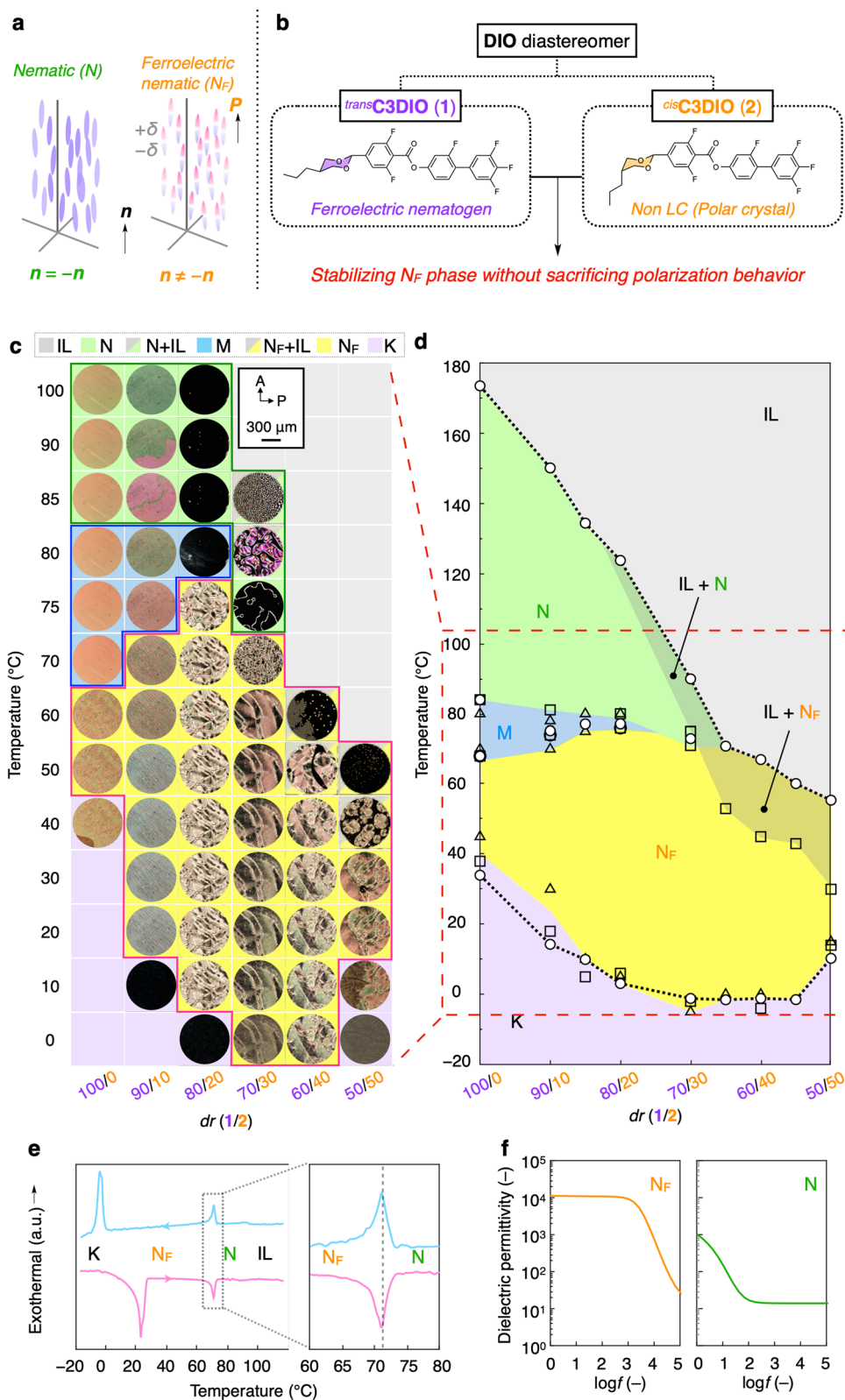


Fig. 1 Diastereomeric-controlled ferroelectric nematic system. **a** Schematic illustration of nematic and ferroelectric nematic phases. **b** Chemical structures of DIO diastereomer: *trans*-C3DIO (**1**) and *cis*-C3DIO (**2**). **1** and **2** have dipole moment of 9.36 and 9.04 D, respectively. **c** Evolution of polarized optical microscope images, which were taken under the crossed polarizers, of the mixture **1/2** with various *dr* (100/0–50/50). Thickness: 13 μm . **d** A phase diagram of the mixture **1/2** as a function of *dr* and temperature. Symbols represent the phase transition temperature determined by differential scanning calorimetry (circle), polarized optical microscopy (square) and XRD (triangle) studies. IL isotropic liquid, N nematic, M mesophase, N_F ferroelectric nematic, K crystal. The coexistence area is indicated by gray shadow. **e** DSC curves of the mixture **1/2** with *dr* (70/30) on cooling (upper line) and heating (bottom line). The bottom panel denotes the enlarged temperature range between 60–80 $^\circ\text{C}$, in which a good match of temperatures due to the N_F -N phase transition (ca. 72 $^\circ\text{C}$) on cooling and heating because of a very weak 1st order or 2nd order phase transition. Temperature recorded on DSC was calibrated using a reference (8CB) exhibiting 2nd order phase transition (SmA-N). **f** Dielectric permittivity as a function of frequency in N_F phase (44 $^\circ\text{C}$, left) and N phase (120 $^\circ\text{C}$, right) for the mixture **1/2** with *dr* (90/10).

strong enough to withstand a thermal fluctuation ($k_B T$), is the most important to emerge from the N_F phase^{35,36}. This unique N_F phase has been ascertained in specific molecules as a 1,3-dioxane-tethered fluorinated molecule (DIO)³, a pear-shaped molecule (RM734)^{1,2}, a fluorinated molecule bearing a terminal cyano group (UUQU-4-N)¹⁴, and other generics^{13,21,24} with very large μ (i.e., >9 Debye). However, although the present systemized molecular parameters, including μ , oblique dipole angle, and geometrical aspect ratio of a molecular shape, are confirmed for the N_F emergence, the effects on the phase sequence passing the N_F phase have not been considered. The archetypal phase behavior of N_F molecules is described as follows: (1) DIO experiences three mesophases: the N–M– N_F phase transition (i.e., M is antiferroelectric N, SmZ_A, or N_s with periodic density modulation in the direction perpendicular to **n**; the nomenclature is under debate^{21,25,33}); (2) RM734 exhibits the N– N_F phase transition that corresponds with the ferroelectric–ferroelastic phase transition seen in inorganic solids;⁹ and (3) the latest key is UUQU-4-N showing the direct N_F phase transition from isotropic liquid (IL) (i.e., IL– N_F phase transition observed in some molecules)^{21,24}. In most cases, the N_F phase is thermodynamically unstable below room temperature, irrespective of a single molecule or LC blends. Considering the results of the single-crystal X-ray diffraction^{4,21,24}, the two adjacent N_F molecules with a synparallel arrangement may flip each other, destructing the N_F state and undergoing crystallization below room temperature. Under this circumstance, the control of the phase sequences involving the N_F emergence and the successful way of stabilizing N_F remain ambiguous despite huge efforts on the design and development of new N_F -LC molecules based on molecular parameters. Note that a new-found ferroelectric state, that is, a uniaxial ferroelectric smectic A (SmA_F) phase^{37,38} that appears just below the N_F phase, just emerged, offering an important clue. SmA_F looks highly correlated with the N_F phase; hence, the smectic cluster floating in the N_F media may influence the N_F phase characteristic.

In this work, we report a ferrofluid matter engineering concept based on the dipole equivalent for controlling the N_F phase transition and its possible impact to cluster formation. Very recently, almost the same diastereomeric system had been coincidentally introduced by another group; however, the mechanism behind this well-controlled N_F phase has remained unknown³⁹. In this study, we focus on the nanoscopic structure in the present diastereomeric binary system and discuss the alteration of the N_F phase transition in terms of the cybotactic cluster formation. The result suggests that the molecule exchange with an almost equivalent dipole moment and an analogous structure occurs without reducing the macroscopic polarization. For this strategy, although two components, including a N_F molecule, are treated, the counter molecule need not be liquid crystalline. This point is unique compared to the conventional approach^{22,40,41}. We herein adopt DIO diastereomers, *trans*-DIO (**1**) and *cis*-DIO (**2**), which are a ferroelectric nematogen and a non-liquid crystalline, respectively (Fig. 1b), to investigate the effect of diastereomeric control and the N_F phase structure in view of the X-ray diffraction (XRD) analysis and computer simulation.

Results and discussion

Control of the variant N_F phase transition in *trans/cis*-C3DIO system. A stereoisomer with an equivalent topological structure, but a different geometric configuration, is also known as a diastereomer⁴². C3DIO has a diastereomer because its 1,3-dioxane moiety with alkyl chain can have two geometric configurations. This C3DIO diastereomer (i.e., *trans*-C3DIO (**1**) and *cis*-C3DIO (**2**)) exhibit different physical properties (see Fig. 1b and Supplementary Figs. 1–6 for the characterization data). **1** is a typical ferroelectric nematogen that exhibits the ferroelectric nematic (N_F) phase on cooling³. Despite a similar large dipole moment to **1** ($\mu_1 = 9.36$ D; $\mu_2 = 9.04$ D; see Supplementary Fig. 7), **2** is not an LC material, but a polar crystal (instead of an apolar one like **1**). Supplementary Fig. 8 (Supplementary Data 1 and 2) shows the single-crystal X-ray crystallographic structures of **1** and **2**. If the diastereomeric ratio (*dr*) of **2** in the **1/2** mixture is increased (i.e., exchanging **1** by **2**), the N_F phase is intuitively expected to destabilize because molecule (**2**) may collapse the strong dipole–dipole interaction between the **1**–**1** molecule. Figure 1c and Supplementary Figs. 9–14 depict the polarizing optical microscope images via the variant phase sequence in the diastereomeric mixture (**1/2**). For *dr* (**1/2** = 100/0), the uniform texture (green-highlighted area in the figure) is first changed to an inhomogeneous one (blue-highlighted area in the figure) and finally to a stripe texture because of the polar defect (e.g., 2π twist-wall¹²) (yellow-highlighted area in the figure) during cooling. These three phases are characterized as the N, M, and N_F phases in the order of high to low temperature. With an increasing *dr*, the intermediate M phase vanishes at *dr* = 70/30. Thus, the mixture with *dr* (70/30) experiences the N– N_F phase transition like the common generic N_F molecules, including RM734³⁴. A further increment of *dr* (>60/40) eliminates the N and M phases, and a direct phase transition between isotropic liquid and N_F phase instead occurs. In the case of *dr* = 60/40, small N_F phase droplets emerge in the isotropic liquid and conglomerate, resulting in a complete N_F phase formation. This direct IL– N_F transition type is a scarce case observed in UUQU-4-N, etc.^{14,21,24}. Thus, against expectation, the **2** doping probably contributes to the phase transition control related to the N_F phase stability. The phase diagram of the **1/2** system is constructed (Fig. 1d) to explore the N_F phase stabilization by the diastereomeric control of DIO. The temperature range of the M phase is reduced at *dr* = 90/10. In addition, the N_F phase regime expands to a lower temperature range across the room temperature. This trend is observed when increasing the doping level of **2** up to *dr* = 70/30, which yields the maximum temperature range of the N_F phase. Interestingly, at *dr* = 70/30, the N_F phase still stands at 0 $^\circ\text{C}$, and the wide regime is 80 $^\circ\text{C}$, which is approximately four times larger than that of pure DIO (**1**). More interestingly, the mixture with *dr* = 70/30 exhibits an enantiotropic N_F phase that is thermodynamically stable, unlike the monotropic N_F phase in **1** (Fig. 1e). Similarly, at the regime with a high doping level of **2** (*dr* \geq 40/60), the N_F phase maintains a wide temperature range of \sim 50–20 K

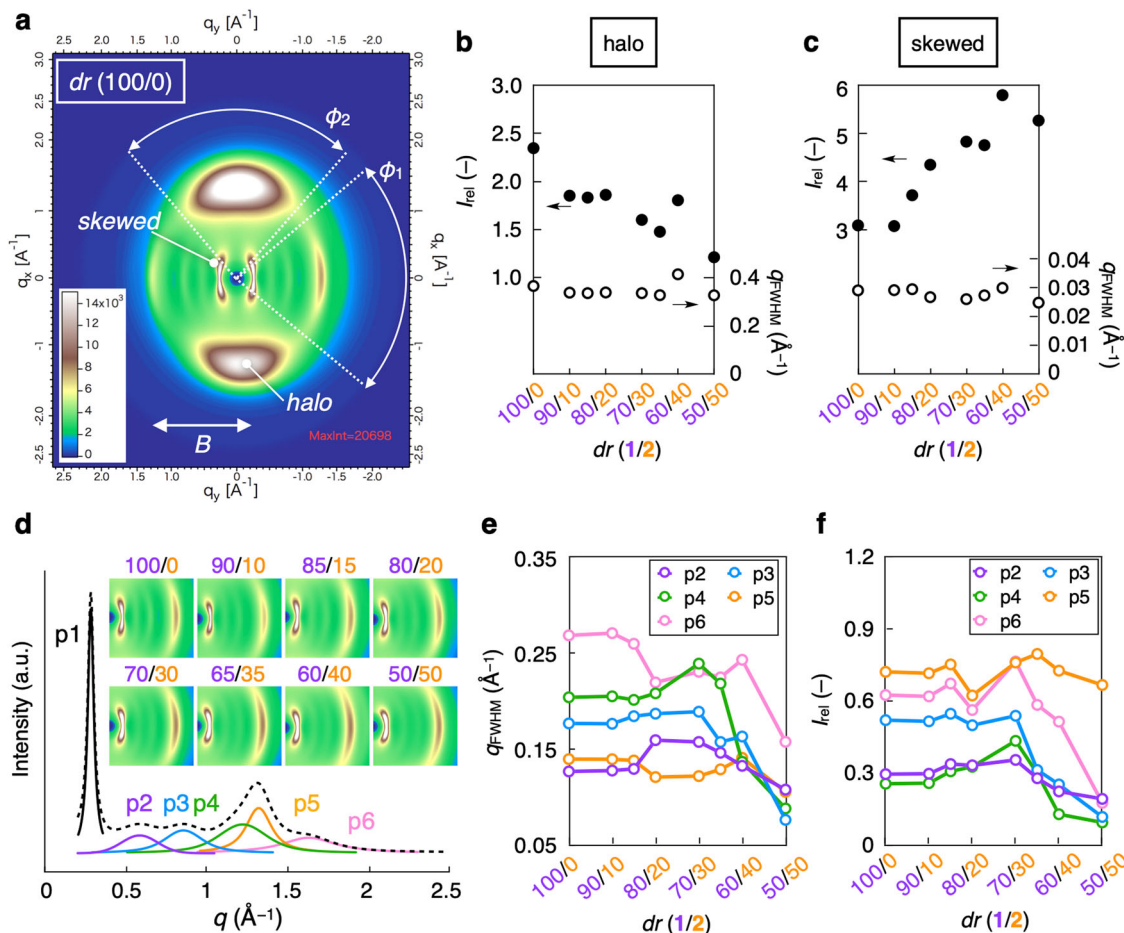


Fig. 2 Wide-angle XRD analysis of the 1/2 mixture with various dr . **a** 2D Wide-angle X-ray diffraction profile of the 1/2 mixture ($dr = 100/0$). The azimuth angle $\varphi_1 = 80^\circ$, $\varphi_2 = 60^\circ$ represents the scanning range for generation of the 1D XRD profile. The value of q_{FWHM} and relative intensity (I_{rel}) as a function of dr for halo (**b**) and skewed peaks (**c**). I_{rel} was calculated by dividing by I_{IL} for halo and skewed peaks. **d** 1D XRD profile of the 1/2 mixture ($dr = 70/30$) with separated peaks (p1–p6). Insets denote the analyzed area for all entries ($dr = 100/0$ – $50/50$). The value of q_{FWHM} (**e**) and relative intensity (I_{rel}) (**f**) as a function of dr for multiple peaks (p2–p6). I_{rel} was calculated by dividing $I_{obs.}$ by the corresponding I_{IL} .

across the room temperature. The dielectric permittivity of the N_F and N phases in the 1/2 system is comparable to that of pure DIO. The N_F and N phases show a dielectric permittivity of the orders of 10^4 and 10 at 1 kHz frequency, respectively (Fig. 1f). Supplementary Fig. 15 depicts the complete DSC curves. Supplementary Table 1 summarizes the corresponding enthalpies.

Structure analysis of the diastereomeric-controlled N_F phase.

As mentioned above, the diastereomeric combination probably alters the nature of the N_F phase transition. We discuss here how the doping level of **2** in **1** affects the N_F phase structure mainly with the aid of a X-ray analysis. Figure 2a displays a two-dimensional (2D) wide-angle XRD (WAXD) pattern of the N_F phase ($T - T_c = -10^\circ\text{C}$) in **1** under the magnetic field ($B \sim 0.5\text{ T}$). Supplementary Fig. 16 provides the complete data. The unique diffraction patterns consist of (i) a pair of skewed peaks corresponding to a molecular length of $\sim 2.2\text{ nm}$ at a small-angle region on the equatorial direction (parallel to **n**), (ii) a series of weak overtone ones spanning the small-to wide-angle region on the equatorial direction, and (iii) halo peaks caused by the intermolecular stacking on the meridional direction (normal to **n**). The WAXD profile is analyzed in detail by performing horizontal and vertical scans within angles $\varphi_1 = 80^\circ$ and $\varphi_2 = 60^\circ$, generating a one-dimensional XRD pattern. Figure 2b, c shows the relative intensity (I_{rel}) and the full width at half maximum (FWHM)

in the q -space (i.e., q_{FWHM}) as a function of dr for the fitted halo/skewed peaks (Supplementary Figs. 17 and 18). For the halo peak, all q_{FWHM} are comparable, while the intensity slightly decreases with the increasing doping level of **2**. By contrast, the q_{FWHM} of the skewed peaks slightly decreases as dr increases. The intensity shows a significant dependence on dr , suggesting that the doping of **2** may promote the cybotactic cluster growth in the N_F phase. The peak separation on the equator direction is also performed, providing peaks (Fig. 2d). For the q_{FWHM} and intensity of peaks p2–p6, although both are on a downward trend at $dr = 60/40$, no remarkable difference is found on any dr (Fig. 2e and f). Let us consider the unusual anisotropic diffraction pattern in the N_F phase of the 1/2 system. For the diffraction on (i) (vide supra), the skewed peak is reflected on the normal cybotaxis, in which an SmC-like stratification exists within the mesogen clusters, floating in the N phase^{43,44}. The diffraction on (ii) may be caused by the anomalously large correlation length in the cybotactic clusters observed in the N phase in a rigid lath molecule⁴⁵. With the aid of molecular dynamics (MD) calculation, Mandel et al. confirmed that a series of weak overtones observed in the N_F phase of RM734 was a consequence of the polar nematic order¹⁸. Considering these important tips, in the 1/2 system, the SmC-type cybotactic cluster may coexist in the N_F phase (Fig. 3a). In this case, the anomalous changes in the diffraction intensity may indicate the growth of the cluster size with a polar order depending on the doping level of **2**.

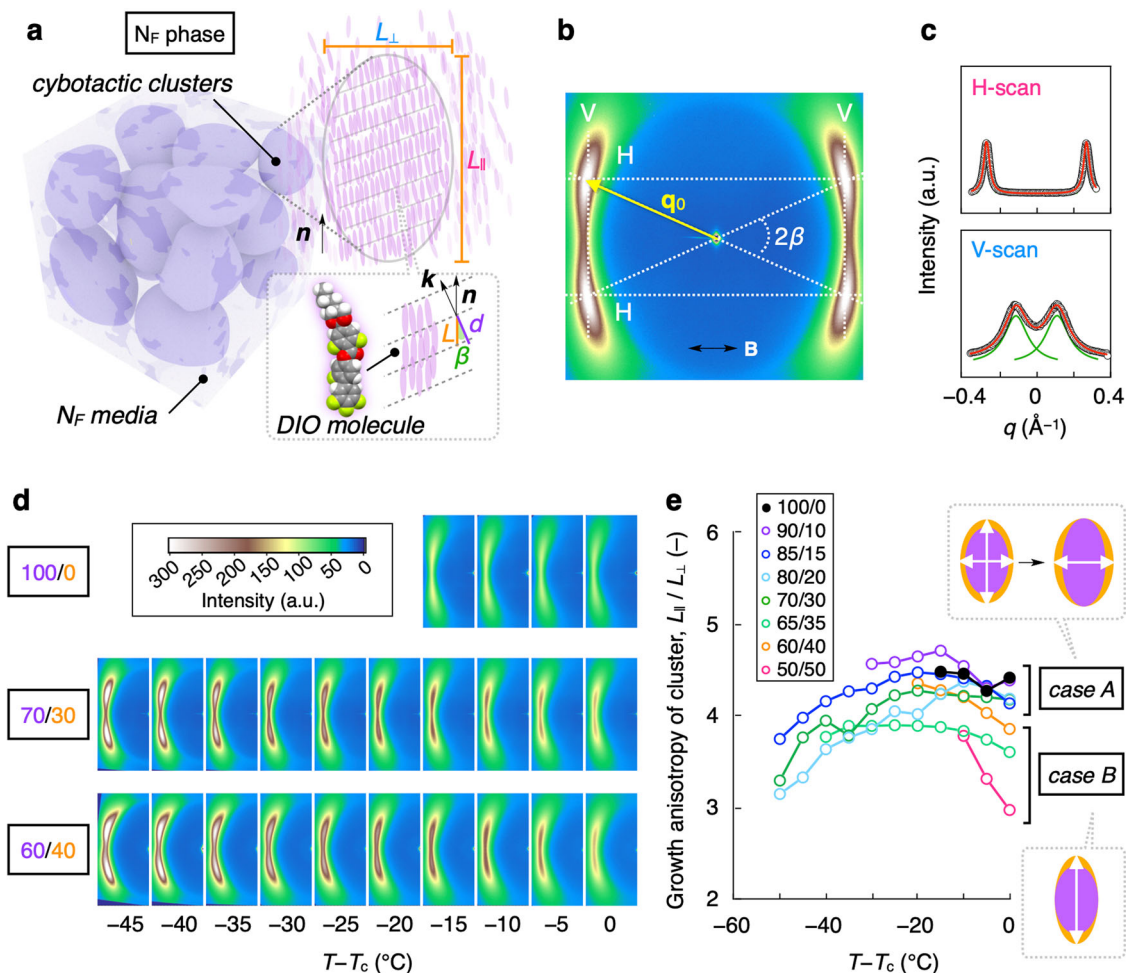


Fig. 3 Characterization of the cybotactic clusters in the diastereomeric-controlled N_F phase. **a** Schematic illustration of the N_F phase of **1** or **1/2** mixture. L_{\parallel} and L_{\perp} are longitudinal and transversal dimension of the cybotactic cluster, respectively. L , d , β denote the molecular length, d -spacing between layers and tilt angle, respectively. **b** Small-angle X-ray scattering profile. A white-colored arrow denotes the direction of the applied magnetic field. The symbols are defined in the text. **c** The horizontal (H) and vertical (V) scans of the four-spot pattern along the H-/V-dash lines indicated in the panel **b**. Intensity profiles $I(\Delta q_{\parallel})$ (upper) and $I(\Delta q_{\perp})$ (bottom) of the small-angle skewed spots measured via the maxima at q_0 long the longitudinal ($\parallel \mathbf{B}$) and transversal ($\perp \mathbf{B}$) direction, respectively. **d** Evolution of the skewed peaks of the **1/2** mixture with $dr = 100/0$, $70/30$ and $60/40$, as a function of the temperature, $T - T_c$. **e** The relationship between growth anisotropy of cluster, $L_{\parallel} / L_{\perp}$ (-) and its temperature-dependent. Inset cartoon depicts the two variation (Case A and case B) of the growth of the cybotactic cluster in the N_F phase.

We analyze in detail the 2D small-angle X-ray scattering (SAXS) patterns in the N_F phase to gain more information on the cluster in the N_F phase. Figure 3a shows a schematic illustration connecting the structural parameters of the SmC-type cybotactic domain. The magnetic field aligns the clusters, in which the director \mathbf{n} is parallel to \mathbf{B} . In the magnetic field, the normal to smectic layer, \mathbf{k} , is randomly distributed on \mathbf{B} at the tilt angle β . As a result, the SAXS profile resulting from this distribution of microscopic SmC-type clusters is observed (Fig. 3b and Supplementary Figs. 19–26). Based on refs. 43,44, we estimated the average size of the cybotactic clusters in the N_F phase and its temperature and dr dependence. The average cluster size can be estimated from the longitudinal ($\parallel \mathbf{B}$) and transversal ($\perp \mathbf{B}$) intensity profiles of the skewed (four-spot) pattern (Fig. 3b). Figure 3c shows an example of the diffraction intensity as a function of $\Delta q_{\parallel,\perp} = \pm |q - q_{\parallel,\perp}|$ of the **1/2** mixture with dr (70/30). The FWHM of $\Delta q_{\parallel,\perp}$ correlates with the anisotropic short-range positional order of the cluster characterized by the correlation length $\xi_{\parallel,\perp}$ (i.e., $\xi_{\parallel,\perp} = \alpha / q_{\text{FWHM},\parallel,\perp}$), where q_{FWHM} is the FWHM at the H-/V-scan profiles and $\alpha = 2$ (for Lorentzian fitting case)⁴³ (Fig. 3b, c). The longitudinal and transversal dimensions of the

cluster, L_{\parallel} and L_{\perp} , are given as $L_{\parallel} = 3\xi_{\parallel}$ and $L_{\perp} = 3\xi_{\perp}$, respectively. Figure 3d shows the temperature evolution of the SAXS pattern with various dr . The four-spot pattern emerged below the critical point (T_c) for the **1/2** mixtures with various dr (100/0–50/50), indicating the presence of the SmC-type cybotactic cluster over the entire range of the N_F phase. With an increasing doping level of **2**, the four-spot contrast tends to be strong, and its intensity drastically increases. From the H-/V-scan profiles of the **1/2** mixtures with various dr (100/0–50/50), we estimate the corresponding L_{\parallel} and L_{\perp} as a function of temperature (Supplementary Fig. 27). For the **1/2** mixtures with high dr , L_{\parallel} and L_{\perp} monotonically increase with a similar slope toward the low temperature. The L_{\parallel} value is significantly elevated compared to L_{\perp} in a series of **1/2** with low dr (>65/35). This result indicates that the growth anisotropy of the cluster (L_{\parallel}/L_{\perp}) should be different with respect to dr of the **1/2** mixtures. Figure 3e evidently shows the striking difference in the cluster growth process. In Case A (up to $T - T_c \sim -30$ °C), the cluster almost isotropically grows and tends to grow transversally beyond the temperature. By contrast, in Case B, a longitudinal cluster growth tendency is observed over the entire N_F phase range. Case B

occurs in the 1/2 mixture with dr ($>65/35$), which experiences a direct IL- N_F phase transition. A similar tendency is observed in UUQU-4-N exhibiting the direct IL- N_F phase transition, in which SmA-like cybotactic cluster coexists in the N_F phase (Supplementary Fig. 28). Thus, the cybotactic cluster in a series of molecules showing the direct IL- N_F phase transition may inherently grow, irrespective of the cybotactic cluster types, via Case B. We next investigate the internal molecular environment in the cluster. The left panel in Fig. 4a is a schematic illustration of the SmC-like stratification within the cluster in the N_F phase with the dr variation at a fixed temperature ($T - T_c = -10^\circ\text{C}$). At $dr = 100/0$, the constituent molecules (**1**) arranged in a smectic layer with the tilt angle $\beta = 24.9^\circ$ (Supplementary Fig. 29) are occupied in the cluster (the left panel in Fig. 4a). With the increasing doping of **2**, the substitution of **1** leads to the generation of scrambled dipoles of **1** and **2** with a changing cluster anisotropy (the middle and right panels in Fig. 4a). At $dr = 50/50$, the majority of clusters is colonized by equimolar molecules. Although β is nonlinearly increased by cooling, reflecting on the SmC feature at each dr , the β value at a fixed temperature is slightly reduced to 19.5° (Supplementary Fig. 29) with the increasing dr . Considering the cybotactic cluster volume (i.e., $L_{\parallel} \times L_{\perp} \times L_{\perp}$), we estimate the average molecular numbers in the cluster of a series of 1/2 mixtures. The average molecular numbers in the longitudinal (N_{\parallel}) or transversal (N_{\perp}) dimension are given as follows:

$$N_{\parallel} = L_{\parallel}/l = 3\xi_{\parallel}/l,$$

$$N_{\perp} = L_{\perp}/w = 3\xi_{\perp}/w,$$

where l and w are the molecular length (ca. 2.23 nm) of DIO and the typical intermolecular distance (ca. 0.47 nm), respectively. The average molecular numbers (\bar{N}) in the cluster are expressed as $N_{\parallel} \times N_{\perp} \times N_{\perp}$. In the case of **1** at $T - T_c = -10^\circ\text{C}$, \bar{N} is calculated as 1036 (i.e., one thousand molecules are occupied in the cluster). Figure 4b summarizes the estimated \bar{N} for all the 1/2 series as a function of the temperature. At a low dr regime ($<70/30$), the \bar{N} monotonically increases and reaches approximately 2000. By contrast, the 1/2 series with a high dr regime ($\geq 70/30$) expresses the tendency of a nonlinear increment of \bar{N} reaching to ca. 2000–4000. Figure 4c highlights the relationship at $T - T_c = -10^\circ\text{C}$. The \bar{N} value increases at the dr threshold (85/15), being 1.5–2 times at the maximum dr . Interestingly, the dr dependence of enthalpy related with the phase transition via the N_F phase shows a quite similar relationship between \bar{N} and dr (Fig. 4d). This suggests that the anomalous latent heat has a strong association with the formation of the cybotactic cluster and its size. At the dr threshold (70/30), two regimes (i.e., IL-N-M- N_F and IL-(N)- N_F) are also classified. The dr threshold shows a good agreement with the dr classifying cases, depicting the cluster growth trend in Fig. 3e.

We assess the cluster model validation in the N_F phase for the 1/2 system by performing an MD simulation using all-atom models with GROMACS 2020.5. Here we simulate four systems: compound **1** arranged all in parallel (**System 1**) and half in anti-parallel (**System 2**) and 50:50 compositions of **1** and **2** all in parallel (**System 3**) and half in anti-parallel (**System 4**). The initial structures are built with six layers containing 100 molecules each. Hence, the total number of molecules in the simulation box is 600. Supplementary Note 1 provides the relevant details for this. Figure 4e compares the time-averaged total energy of the four systems and the corresponding MD snapshots in the N_F regime ($T - T_c = -15^\circ\text{C}$). The calculated energies (G) of **Systems 1** and **2** are $\sim 6087 \text{ kcal mol}^{-1}$ and $\sim 7285 \text{ kcal mol}^{-1}$, respectively. Thus, the parallel (polar) orientation may predominately occur in the

1-only system. This result corresponds with that of previous reports^{8,18}. By a sharp contrast, the time-averaged total energies of **Systems 3** and **4** are extremely lower (i.e., $G_{(\text{System } 3)} = -6879 \text{ kcal mol}^{-1}$ and $G_{(\text{System } 4)} = -6306 \text{ kcal mol}^{-1}$); hence, it is natural to consider that the doping of **2** stabilizes the system. Interestingly, closely looking at the MD simulation snapshots shows a pairing of **1** and **2**, which means a plausible dimerization (Supplementary Fig. 33) confirmed by the peak differences on the 2D radial distribution function profiles of **1** only, **2** only, and both **1** and **2** in the one layer for **System 3** (Supplementary Fig. 37). The possibility of dimerization is also discussed through the density functional theory calculation⁴⁶ (Supplementary Note 1, Supplementary Table 2, Supplementary Figs. 30–32, 34–36, and 38–39). A rough estimate of the energetic difference of the pair interaction in **Systems 3** and **4** provided $573/300 \sim 2 \text{ kcal mol}^{-1}$, which is comparable with the thermal agitation energy above the room temperature (e.g., $n_A k_B T \sim 2.4 \text{ kcal mol}^{-1}$ at 300 K). The total energy in MD tends to be reduced by the size limitation of the simulation box. It looks reasonable that the polar orientation of the 1–2 dimers in a cluster is energetically preferable than the apolar 1–2 configuration. The tilt angles (β) of **Systems 1** and **3** are well accorded with those obtained by the X-ray analysis (Fig. 4e and Supplementary Fig. 29). Hence, the MD simulation results strongly support our polar configuration model.

Polarization behavior of the diastereomeric-controlled N_F phase.

As an early prediction, the replacement of the N_F molecule (**1**) with a non-LC molecule (**2**) will probably cause a destruction of the strong dipole–dipole interaction between the 1–1 molecule, such that the N_F phase should be destabilized. Contrary to expectation, by diastereomeric control using **2**, we succeeded in realizing the N_F state operating over an extended temperature range from 80°C to 0°C and controlled various phase transition sequences, as mentioned above. If the diastereomeric-controlled N_F phase is a truly stabilized state, the corresponding polarization properties should also be equal to or greater than the original ones. Accordingly, we investigated the polarization behavior of the N_F phase 1/2 system by dielectric relaxation, P - E hysteresis, and SHG studies. The comparable temperature was fixed to -10°C of $T - T_c$. Figure 5a shows the dielectric permittivity as a function of the frequency of the 1/2 mixture with various dr . All mixtures exhibited a similar order of dielectric permittivity (i.e., 10^4), and the corresponding relaxation peak moved toward a low frequency range. Supplementary Figs. 40 and 41 provide the complete data for this. With an increasing doping level of **2**, although the relaxation frequency (f_r) decreased, the dielectric strength order was maintained (Fig. 5b). The dr dependence of frequency was discussed in Supplementary Note 2 and Supplementary Fig. 46. For the P - E hysteresis variation, typical parallelogram-like P - E loops that often appear in ferroelectrics were obtained in all mixtures (Fig. 5c). The corresponding coercive electric field was increased toward a high dr . Notably, the polarization density ($P \sim 4 \mu\text{C cm}^{-2}$) of the 1/2 mixture was increased, and the maximum P was marked at $dr = 70/30$ (Fig. 5d). Supplementary Fig. 42 provides the complete data on the P - E hysteresis. The SHG is quickly recognized as a powerful tool for confirming the macroscopic polar order and its symmetry of individual nanostructures. Figure 5e presents the SHG as a function of the temperature under the electric field ($0.7 \text{ V } \mu\text{m}^{-1}$) for all mixtures. Supplementary Fig. 43 presents the optical setup. For all mixtures, the high SHG activity was observed in the N_F phase range. For example, the SHG profile at $dr = 70/30$ was set as a master curve. The other SHG profiles coincided well with the master curve. Figure 5f depicts the dr -dependent SHG of all mixtures. The SHG intensities at $dr \geq 90/10$ were larger than that

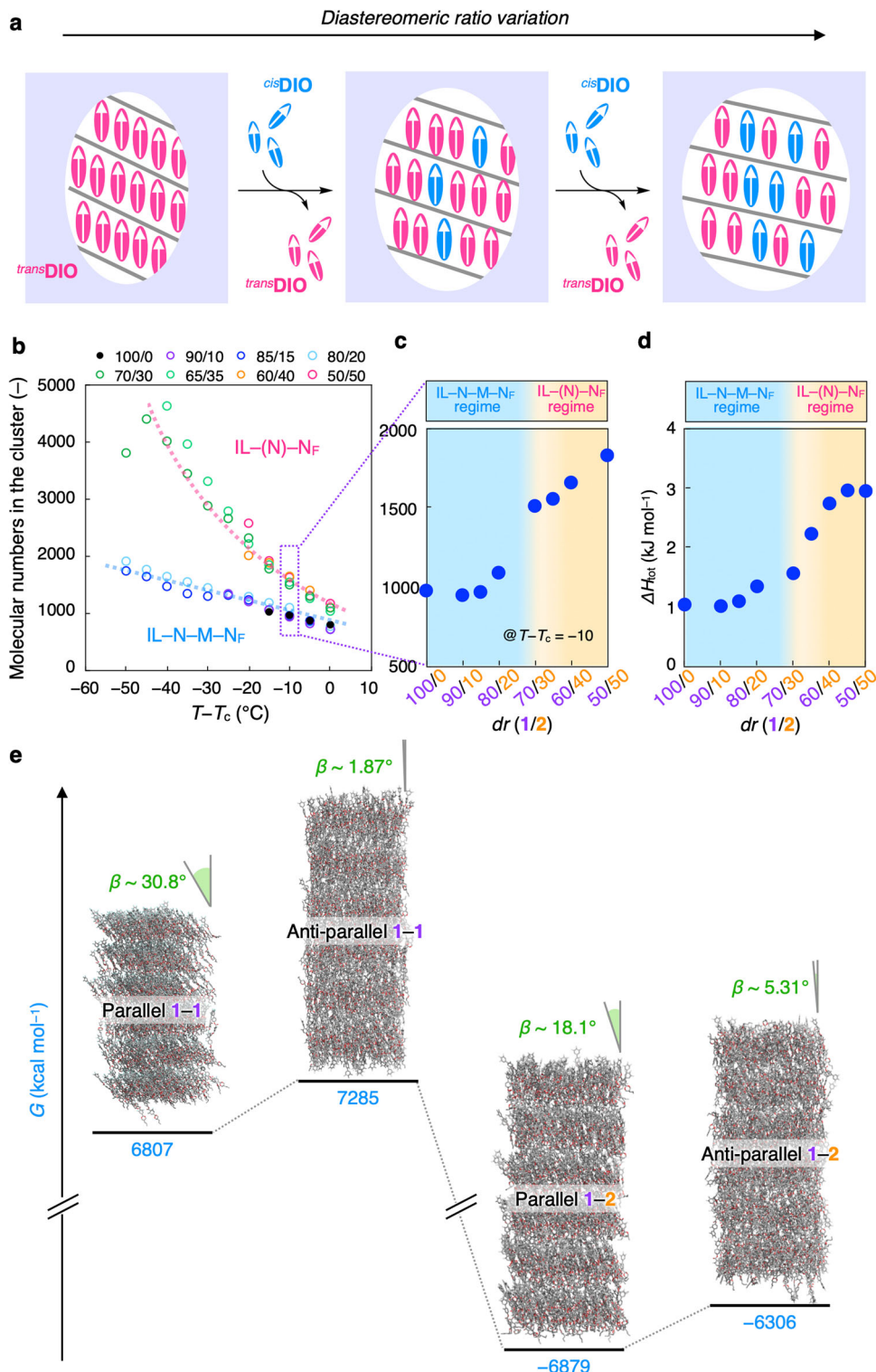


Fig. 4 Clustering effect on the evolution of phase sequence. **a** The schematic illustration of the growth process of the cybotactic cluster in the N_F phase for $1/2$ mixture. The exchange of cisDIO with transDIO promotes the anisotropic cluster growth. **b** The average molecular numbers in the cluster (\bar{N}) as a function of $T - T_c$ of the $1/2$ mixture with various dr (100/0–50/50). **c** The corresponding \bar{N} as a function of dr ($T - T_c = -10$ °C). **d** The relationship between latent heat (ΔH) and dr at $T - T_c = -10$ °C. Note: two distinct section of the phase transition types are indicated by color bands: IL-N-M- N_F regime (blue), IL-(N)- N_F regime (orange) in the panel **c** and **d**. **e** Energy diagram of the N_F phase in $1/2$ system generated by MD simulation. The snapshots (after 300 ns equilibration run) of four system consisting of parallel **1-1**, anti-parallel **1-1**, parallel **1-2** and anti-parallel **1-2** dimers obtained by all-atom MD simulation (for **1-1** dimer, 323 K; for **1-2** dimer, 288 K) are inserted. β denotes the average tilt angle of molecules in a smectic layer. The bottom values are the average total energy (simulation time: 200–300 ns).

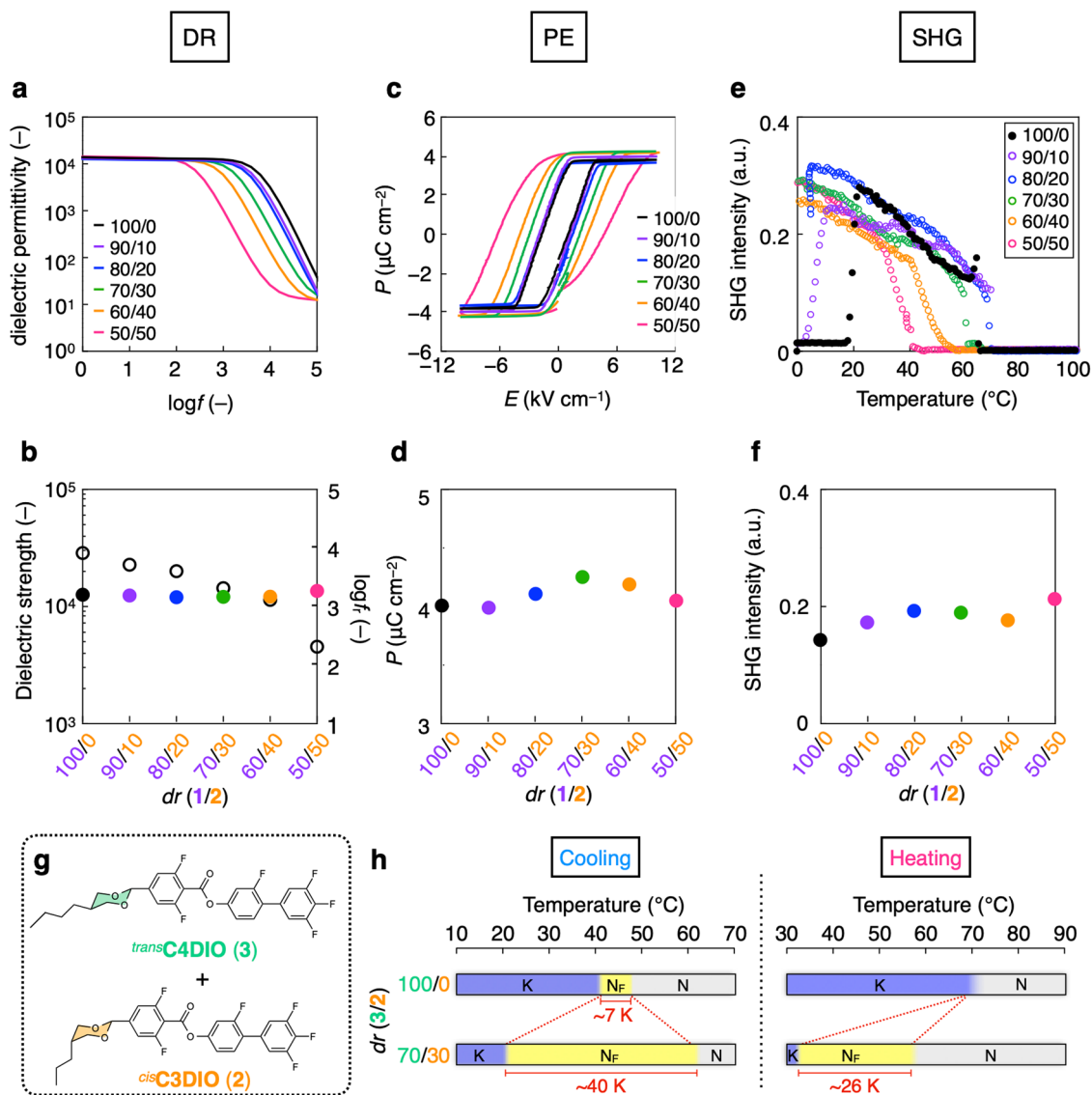


Fig. 5 Polarization behavior of the 1/2 mixture with various dr . **a** Dielectric spectra. **b** Dielectric strength and the corresponding relaxation frequency ($\log f_r$) vs. dr ($T - T_c = -10$ °C). **c** P - E hysteresis loops ($f = 200$ Hz, $V_{\max} = 10$ kV cm $^{-1}$). **d** Polarization density vs. dr ($T - T_c = -10$ °C). **e** Field-induced p -in/ p -out SHG at a 45° incident angle as a function of temperature (0.7 V μm^{-1}). **f** The SHG intensity vs. dr ($T - T_c = -10$ °C). Notes: LC-cell conditions: thickness of 13 μm ; silanized coated ITO electrode (5×10 mm) for dielectric and P - E hysteresis studies; thickness of 5 μm ; silanized coated baked-ITO electrode (4×5 mm) for SHG study. **g** Chemical structures of *trans*C4DIO (**3**) and *cis*C3DIO (**2**). **h** Temperature-dependent phase behaviors of the **3/2** mixture with $dr = 100/70$ (upper) and $dr = 70/30$ (bottom) on cooling and heating.

at $dr = 100/0$. Hence, the combined results provided evidence that the diastereomeric-controlled N_F phase was in a stabilized N_F state without sacrificing the polarization behavior. The counter molecule **2** against **1** plays an important role as a N_F phase stabilizer.

Finally, we demonstrated the potential of a stabilizer (**2**) for boosting the temperature range of the N_F phase, even in another host N_F molecule. We selected herein *trans*C4DIO (**3**) that exhibits a monotropic N_F phase, of which the temperature range is very narrow (~ 7 K) (Fig. 5g, h and Supplementary Fig. 44a). Molecule **3** was blended with a stabilizer **2** to yield the **3/2** mixture with $dr (=70/30)$. As a result, the temperature range of the N_F phase was extremely extended from 7 to 40 K across the room temperature. Surprisingly, the N_F phase was stably operated with a temperature range of 26 K on heating (i.e., enantiotropic N_F phase) (Fig. 5g, h and Supplementary Fig. 44b). Supplementary Fig. 45 summarizes the N_F phase characterization in the **3/2** mixture with $dr (=70/30)$.

Conclusion

In conclusion, we demonstrate herein the alteration of the N_F phase transition and the nano-cluster formation in the diastereomeric mixture of *trans*DIO (**1**) and *cis*DIO (**2**). In the 1/2 mixtures with various diastereomeric ratios, we successfully tune three types of phase sequences passing the N_F phase, namely the IL- N - M - N_F , IL- N - N_F , and IL- N_F phase transitions. The 1/2 mixture with $dr = 70/30$ exhibited an enantiotropic N_F phase with a wide temperature range (~ 50 K) across the room temperature. The SAXS analysis of the 1/2 mixture clearly and evidently showed that the cybotactic cluster exists in the N_F phase, and the anisotropic growth of the cluster dominates the phase sequence types. The computer simulation clarified that in the nano-cluster, the substitution of **1** with **2** without energetic penalty in the polar configuration was allowed, and **1**-**2** (parallel polar arrangement) was the energetically most stable configuration in another pair case. Furthermore, the combination of

dielectric, P - E hysteresis, and SHG studies confirmed that the diastereomeric-controlled N_F phase had a similar macroscopic polarization, indicating that replacing **1** with **2** stabilized the N_F phase without sacrificing its macroscopic polarization. This model was also adapted in the monotropic N_F molecule, trans-C4DIO, collaborating with **2**. The results led to the enantiotropic nature and an extended temperature range of the N_F phase (24 K) on heating. We believe that this proposed approach allows for a new scope of N_F matter engineering and/or new theories to be explored and conceptualized.

Method

General and materials. See Supplementary Methods

Fabrication methods for liquid crystalline (LC) cells. Sandwich-type electrical cell (5 and 13 μm -thickness): Pre-treated ITO-coated glass plates (EHC model D-type, electrode area: $5 \times 10 \text{ mm}^2$) were silanized with a silane coupling reagent (octadecyltriethoxysilane, TCI) at 120 °C for 2 h, and then were rinsed with EtOH and ultrapure water. The two resulting glass plates were fixed with drops of an UV-curable glue using polymeric beads (micropearl, SEKISUI) as a spacer. The cell gap was estimated by capacitance of the empty cell. For SHG measurement, we used ITO-coated glass plates (GEMOATEC, electrode area: $4 \times 5 \text{ mm}^2$), which was pre-baked at 400 °C for 1 h in the electronic furnace (SUPER100T, SHIROTA) prior to glass washing.

Preparation and measurement methods for LC cells. Preparation of LC mixtures (1/2 or 3/2): the protocol is as follows: 1) a compound was added in a vial (6 mL) and precisely weighted using an electronic balance (MSE2.7 S, sartorius); 2) a chloroform was added into this vial, preparing a mother liquor; 3) Two kind of mother liquors (chloroform solution of **1** (or **3**) and **2**) were mixed with appropriate concentration using an electronic micro-pipet (eVol, SGE Analytical Science); 4) the solution mixture was vortexed and then evaporated at 40 °C in a jet oven overnight; 5) the resulting mixture was dried in vacuo at room temperature for 3 h and then mechanically stirred at 120 °C by a magnetic stirrer followed by cooling to room temperature.

For experiments: The LC mixture was injected by capillary action into a LC cell (5 μm - and 13 μm -thickness).

Polarized optical microscopy. Polarized optical microscopy were performed on a polarizing microscope (Eclipse LV100 POL, Nikon) with controlling the temperature using a temperature controller and a hot stage (mk2000, INSTEC). Unless otherwise noted, the sample temperature was controlled using INSTEC model mk2000 temperature controller and a liquid nitrogen cooling system pump (LN2-P/LN2-D2, INSTEC).

Differential scanning calorimetry. Differential scanning calorimetry was performed on a calorimeter (DSC30, Mettler-Toledo). Cooling/heating profiles were recorded and analyzed using the Mettler-Toledo STARE software system.

Dielectric spectroscopy. Dielectric relaxation spectroscopy was performed ranging between 1 Hz and 1 MHz using an impedance/gain-phase analyzer (SI 1260, Solartron Metrology) and a dielectric interface (SI 1296, Solartron Metrology). Prior to starting measurement of the LC sample, the capacitance of the empty cell was determined.

P - E hysteresis measurements. P - E hysteresis measurements were performed in the temperature range of the N_F phase under a triangular-wave electric field (10 kV cm^{-1} , 200 Hz) using FCE system (TOYO Corporation), which equipped with an arbitrary waveform generator (2411B), a IV/QV amplifier (model 6252) and a simultaneous A/D USB device (DT9832).

SHG measurement. The SHG investigation was carried out using a Q-switched Nd:YAG laser (FQS-400-1-Y-1064, Elforlight) at $\lambda = 1064 \text{ nm}$ with a 5 ns pulse width (pulse energy: 400 μJ) and a 2 kHz repetition rate. The primary beam was incident on the LC cell following by the detection of the SHG signal. The electric field was applied normal to the LC cell. The optical setup is shown in Supplementary Fig. 43.

Wide-angle X-ray diffraction (WAXD) and small-angle X-ray scattering (SAXS) analyses. Two-dimensional WAXD and SAXS measurements were carried out at BL38B1 in the SPring-8 synchrotron radiation facility (Hyogo, Japan). The samples held in a glass capillary (1.5 mm in diameter) were measured under a magnetic field at a constant temperature using a temperature controller and a hot stage (mk2000, INSTEC) with high temperature-resistance neodymium magnets ($\sim 0.5 \text{ T}$, MISUMI). The scattering vector q ($q = 4\pi \sin\theta / \lambda$; 2θ and $\lambda =$ scattering angle and wavelength of an incident X-ray beam [1.0 Å (for WAXD) and 0.95 Å (for SAXS)]) and position of an incident X-ray beam on the detector were calibrated using several orders of layer diffractions from silver behenate ($d = 58.380 \text{ Å}$). The sample-to-detector distances were 2.5 m (for

WAXD) and 0.29 m (for SAXS), where acquired scattering 2D images were integrated along the Debye-Scherrer ring by using software (Igor Pro with Nika-plugin), affording the corresponding one-dimensional profiles.

Data availability

The authors declare that the data supporting the findings of this study are available within the paper and its supplementary information files. All other information is available from the corresponding authors upon reasonable request.

Received: 2 June 2022; Accepted: 28 October 2022;

Published online: 11 November 2022

References

- Mandle, R. J., Cowling, S. J. & Goodby, J. W. A nematic to nematic transformation exhibited by a rod-like liquid crystal. *Phys. Chem. Chem. Phys.* **19**, 11429–11435 (2017).
- Mandle, R. J., Cowling, S. J. & Goodby, J. W. Rational design of rod-like liquid crystals exhibiting two nematic phases. *Chem. Eur. J.* **23**, 14554–14562 (2017).
- Nishikawa, H. et al. A fluid liquid-crystal material with highly polar order. *Adv. Mater.* **29**, 1702354 (2017).
- Mertelj, A. et al. Splay nematic phase. *Phys. Rev. X* **8**, 041025 (2018).
- Mandle, R. J. & Mertelj, A. Orientational order in the splay nematic ground state. *Phys. Chem. Chem. Phys.* **21**, 18769–18772 (2019).
- Mandle, R. J., Cowling, S. J. & Goodby, J. W. Chemically induced splay nematic phase with micron scale periodicity. *Soft Matter* **16**, 324–329 (2020).
- Rosseto, M. P. & Selinger, J. V. Theory of the splay nematic phase: Single versus double splay. *Phys. Rev. E* **101**, 052707 (2020).
- Chen, X. et al. First-principles experimental demonstration of ferroelectricity in a thermotropic nematic liquid crystal: polar domains and striking electro-optics. *Proc. Natl Acad. Sci. USA* **117**, 14021–14031 (2020).
- Sebastián, N. et al. Ferroelectric-ferroelastic phase transition in a nematic liquid crystal. *Phys. Rev. Lett.* **124**, 037801 (2020).
- Kats, E. I. Stability of the uniform ferroelectric nematic phase. *Phys. Rev. E* **103**, 012704 (2021).
- Mandle, R. J., Cowling, S. J. & Goodby, J. W. Structural variants of RM734 in the design of splay nematic materials. *Liq. Cryst.* **48**, 1780–1790 (2021).
- Chen, X. et al. Polar in-plane surface orientation of a ferroelectric nematic liquid crystal: Polar monodomains and twisted state electro-optics. *Proc. Natl. Acad. Sci. USA* **118**, e2104092118 (2021).
- Saha, R. et al. Multiple ferroelectric nematic phases of a highly polar liquid crystal compound. *Liq. Cryst.* <https://doi.org/10.1080/02678292.2022.2069297> (2022).
- Manabe, A., Bermer, M. & Kraska, M. Ferroelectric nematic phase at and below room temperature. *Liq. Cryst.* **48**, 1079–1086 (2021).
- Nishikawa, H. & Araoka, F. A new class of chiral nematic phase with helical polar order. *Adv. Mater.* **33**, 2101305 (2021).
- Madhusudana, N. V. Simple molecular model for ferroelectric nematic liquid crystals exhibited by small rodlike mesogens. *Phys. Rev. E* **104**, 014704 (2021).
- Sebastián, N. et al. Electrooptics of mm-scale polar domains in the ferroelectric nematic phase. *Liq. Cryst.* **48**, 2055–2071 (2021).
- Mandle, R. J., Sebastián, N., Martínez-Perdiguero, J. & Mertelj, A. On the molecular origins of the ferroelectric splay nematic phase. *Nat. Commun.* **12**, 4962 (2021).
- Caimi, F. G. et al. Surface alignment of ferroelectric nematic liquid crystals. *Soft Matter* **17**, 8130–8139 (2021).
- Feng, C. et al. Electrically tunable reflection color of chiral ferroelectric nematic. *liquid crystals. Adv. Opt. Mater.* **9**, 2101230 (2021).
- Brown, S. et al. Multiple polar and non-polar nematic phases. *Chem. Phys. Chem* **22**, 2506–2510 (2021).
- Chen, X. et al. Ideal mixing of paraelectric and ferroelectric nematic phases in liquid crystals of distinct molecular species. *Liq. Cryst.* <https://doi.org/10.1080/02678292.2022.2058101> (2022).
- Rudquist, P. Revealing the polar nature of a ferroelectric nematic by means of circular alignment. *Sci. Rep.* **11**, 24411 (2021).
- Pociecha, D. et al. Intrinsically chiral ferromagnetic liquid crystals: An inversion of the helical twist sense at the chiral nematic – Chiral ferromagnetic phase transition. *J. Mol. Liq.* **361**, 119532 (2022).
- Chen, X. et al. Antiferroelectric smectic ordering as a prelude to the ferroelectric nematic: introducing the smectic Z_A phase. Preprint at <https://doi.org/10.48550/arXiv.2112.14222> (2021).
- Basnet, B. et al. Domain patterns with paired soliton walls stabilized by polar surface interactions in a ferroelectric nematic liquid crystal. *Nat. Commun.* **13**, 3932 (2022).

27. Máthé, M. T., Buka, A., Jákl, A. & Salamon, P. Ferroelectric nematic liquid crystal thermomotor. *Phys. Rev. E* **105**, L052701 (2022).
28. Nishikawa, H., Sano, K. & Araoka, F. Anisotropic fluid with phototunable dielectric permittivity. *Nat. Commun.* **13**, 1142 (2022).
29. Emelyanenko, A. V. et al. Emergence of paraelectric, improper antiferroelectric, and proper ferroelectric nematic phases in a liquid crystal composed of polar molecules. *Phys. Rev. E* **105**, 064701 (2022).
30. Etxebarría, J., Folcia, C. L. & Ortega, J. Generalization of the Maier-Saupe theory to the ferroelectric nematic phase. *Liq. Cryst.* <https://doi.org/10.1080/02678292.2022.2055181> (2022).
31. Folcia, C. L. et al. The ferroelectric nematic phase: an optimum liquid crystal candidate for nonlinear optics. *Liq. Cryst.* <https://doi.org/10.1080/02678292.2022.2056927> (2022).
32. Barboza, R. et al. Explosive electrostatic instability of ferroelectric liquid droplets on ferroelectric solid surfaces. *Proc. Natl Acad. Sci. USA* **119**, e2207858119 (2022).
33. Sebastián, N., Čopič, M. & Mertelj, A. Ferroelectric nematic liquid crystalline phases. *Phys. Rev. E* **106**, 021001 (2022).
34. Mandle, R. J. A new order of liquids: polar order in nematic. *liquid crystals. Soft Mater* **18**, 5014–5020 (2020).
35. Lavrentovich, O. D. Ferroelectric nematic liquid crystal, a century in waiting. *Proc. Natl. Acad. Sci. USA* **117**, 14629–14631 (2020).
36. Fischer, V. E. & Born, M. Über anisotrope Flüssigkeiten. Versuch einer Theorie der flüssigen Kristalle und des elektrischen Kerr-Effekts in Flüssigkeiten. *Sitzungsber. Sitzungsber. Preuss. Akad. Wiss.* **30**, 614–650 (1916).
37. Kikuchi, H. et al. Fluid layered ferroelectrics with global $C_{\infty v}$ symmetry. *Adv. Sci.* **9**, 2202048 (2022).
38. Chen, X. et al., Observation of a uniaxial ferroelectric smectic A phase. Preprint at <https://doi.org/10.48550/arXiv.2206.12965> (2022).
39. Zhou, J., Xia, R., Huang, M. & Aya, S. Stereoisomer effect on ferroelectric nematics: stabilization and phase behavior diversification. *J. Mater. Chem. C* **10**, 8762–8766 (2022).
40. Kikuchi, H. et al. A novel liquid crystalline phase with giant dielectric permittivity–ferroelectric nematic phase–. In *Abstract Book of Japanese Liquid Crystal Society Online Meeting*. https://doi.org/10.11538/ekitou.2020.0_2102. (2020).
41. Raynes, P. In *Handbook of liquid crystals*, vol. 1 (eds Goodby, J. W., Collings, P. J., Kato, T., Tschierske, C., Gleeson, H., Raynes, P. & Vill, V.) Ch.12 (Weinheim, 2014).
42. Cross, L. C. & Klyne, W. Rules for the nomenclature of organic chemistry. Section E – Stereochemistry. *Pure Appl. Chem.* **45**, 11–30 (1976).
43. Francescangeli, O., Laus, M. & Galli, G. Structure of the nematic mesophase with cybotactic groups in liquid-crystalline poly(urethane-ester)s. *Phys. Rev. E* **55**, 481–487 (1997).
44. Francescangeli, O. & Samulski, E. T. Insights into the cybotactic nematic phase of bent-core molecules. *Soft Matter* **6**, 2413–2420 (2010).
45. Vita, F. et al. Molecular ordering in the high-temperature nematic phase of an all-aromatic liquid crystal. *Soft Matter* **12**, 2309–2314 (2016).
46. Frisch, M. J. et al. Gaussian 09, revision E.01; (Gaussian, Inc., Wallingford, CT, 2009).

Acknowledgements

The authors are grateful to Dr. T. Hikima and Dr. M. Yamamoto (RIKEN, SPring-8 Center) for supporting X-ray measurement in SPring-8 and Dr. H. Sato (RIKEN, CEMS) for allowing us to use a QTOF compact (BRUKER). We wish to thank Mr. M. Kuwayama

(RIKEN, CEMS) for the QTOF-HRMS measurement, and Dr. D. Miyajima (RIKEN, CEMS), Dr. Y. Sasaki (Hokkaido University), Mr. Z. Li (RIKEN, CEMS), and Mr. A. Manabe (ex. Merck KGaA) for fruitful discussions. We would like to thank Merck KGaA for sample contribution (UUQU-4-N). This work was supported by JSPS KAKENHI Grant Numbers JP19K15438 (H.N.), JP19H02537 (G.W.) and JP21H01801 (F.A.), Incentive Research Projects in RIKEN (No. 100689; H.N.) and JST CREST (Grant Number JPMJCR17N1; F.A.), and JST PRESTO (Grant No. JPMJPR20A6; K.S.). The small-/wide-angle X-ray scattering measurements were performed at BL38B1 in SPring-8 with the approval of the RIKEN SPring-8 Center (proposal 20210080). The computations were partially performed at the Research Center for Computational Science, Okazaki, Japan (Project: 21-IMS-C043, 22-IMS-C043).

Author contributions

H.N. conceived the project and performed all the experiments. F.A. co-designed the work. K.S. and F.A. supported XRD measurements and analyses. S.K. and G.W. performed MD and DFT calculations. A.N. synthesized compounds. B.D. helped and analyzed the single crystal XRD. H.N., K.S. and F.A. analyzed data and discussed the results. H.N. and F.A. wrote the manuscript and all authors approved the final manuscript.

Competing interests

The authors declare no competing interests.

Additional information

Supplementary information The online version contains supplementary material available at <https://doi.org/10.1038/s43246-022-00312-9>.

Correspondence and requests for materials should be addressed to Hiroya Nishikawa or Fumito Araoka.

Peer review information *Communications Materials* thanks Pratap Dharmendra Singh, Richard Mandle and the other, anonymous, reviewer(s) for their contribution to the peer review of this work. Primary Handling Editor: Aldo Isidori. Peer reviewer reports are available.

Reprints and permission information is available at <http://www.nature.com/reprints>

Publisher's note Springer Nature remains neutral with regard to jurisdictional claims in published maps and institutional affiliations.



Open Access This article is licensed under a Creative Commons Attribution 4.0 International License, which permits use, sharing, adaptation, distribution and reproduction in any medium or format, as long as you give appropriate credit to the original author(s) and the source, provide a link to the Creative Commons license, and indicate if changes were made. The images or other third party material in this article are included in the article's Creative Commons license, unless indicated otherwise in a credit line to the material. If material is not included in the article's Creative Commons license and your intended use is not permitted by statutory regulation or exceeds the permitted use, you will need to obtain permission directly from the copyright holder. To view a copy of this license, visit <http://creativecommons.org/licenses/by/4.0/>.

© The Author(s) 2022